IEEE Access
Multidisciplinary | Rapid Review | Open Access Journal

Received August 22, 2019, accepted September 10, 2019, date of publication September 16, 2019, date of current version October 3, 2019.

Digital Object Identifier 10.1109/ACCESS.2019.2941562

Design and Implementation of a Clamper-Based and Motor-Driven Capsule Robot Powered by Wireless Power Transmission

JINYANG GAO [1,2] AND GUOZHENG YAN [3]

[1]Science and Technology on Electronic Test and Measurement Laboratory, North University of China, Taiyuan 030051, China
[2]Shanxi Key Laboratory of Advanced Manufacturing Technology, North University of China, Taiyuan 030051, China
[3]Department of Instrument Science and Engineering, Shanghai Jiao Tong University, Shanghai 200240, China

Corresponding author: Jinyang Gao (gjy.1001@163.com)

This work was supported in part by the National Natural Science Foundation of China under Grant 61803347, Grant 61673271, and Grant 81601631, in part by the Shanxi Province Science Foundation for Youths under Grant 201801D221201, in part by the Youth Academic Leader Support Project of North University of China under Grant QX201808, and in part by the Opening Foundation of Shanxi Key Laboratory of Advanced Manufacturing Technology under Grant XJZZ201803.

ABSTRACT This paper proposes a clamper-based and motor-driven capsule robot (CMCR) for exploring the intestinal tract. The CMCR, measuring $\Phi 14$ mm $\times$ 46.8 mm, is composed of a front facing camera, a clamper-based locomotion mechanism (LM), a telemetry circuit, and a solid-cylinder three-dimensional (3-D) receiving coil for wireless power induction. The LM consists of a translational mechanism (TM), a free clamper that can be moved linearly by the TM, and a fixed clamper. The two clampers both employ arc-shaped legs for expanding with diameters that range from 14 mm to 31 mm; and they can cooperate with the TM to simulate active locomotion in two modes. One mode contains four gaits and is used in an almost horizontal intestine, while the other mode contains six gaits and is used when the CMCR moves in a sloped intestine or against intestinal peristalsis. The solid-cylinder 3-D receiving coil is designed with an aim of maximizing its output power within a given available space, which is achieved by optimizing its design parameters with a calculation-based design method. Finally, the CMCR performance is tested: it works properly when powered by the solid-cylinder 3-D receiving coil, and has a satisfactory speed of 6.32 cm/min in a horizontal ex-vivo intestine and 2.69 cm/min in a vertical one. These test results indicate that the CMCR is promising for a minimally invasive intestinal exploration.

INDEX TERMS Capsule robot, locomotion mechanism, solid-cylinder 3-D receiving coil, intestinal exploration.

I. INTRODUCTION

Capsule endoscope has attracted a lot of research interest since the first capsule product M2A was released in 2000 [1], for its promising diagnostic [2] and therapeutic [3], [4] applications in the gastrointestinal (GI) tract in a minimally invasive manner. However, it cannot be controlled directly and consequently has a high miss rate of 20%-30% [5], which makes it solely as an auxiliary inspecting device. This has motivated the development of a capsule robot (CR) that has an active locomotion ability. A variety of CRs have been proposed during the past decade, and they can be roughly classified into two types, depending on the way the active locomotion is realized. One refers to the magnetically-driven type [6]–[11], which exploits the magnetic interaction (traction/rotation) between an onboard permanent magnet and an external magnetic field to realize active locomotion, is mainly used in the large GI cavities. For example, the CRs those exploit the magnetic traction [6]–[8], can realize multi-DOF motion and have been preliminarily used in clinical practice for inspecting a stomach dilated by water. While the CRs those exploit the magnetic rotation [9]–[11], can travel in a liquid-filled tubular environment such as the colon. In addition, the magnetic rotation has also been used for biopsy in a recent study [12]. The other refers to the actuator-based type that employs onboard micro-motors and a couple of mechanisms [13]–[18]. Normally, the actuator-based CR has a larger propulsive force than the magnetically-driven

The associate editor coordinating the review of this manuscript and approving it for publication was Wenbing Zhao.

type, therefore it is more suitable to explore the intestine which is collapsed in its natural state.

For a thorough inspection of the intestine, the actuator-based CR is expected to have two ideal features.

The first feature refers to a complete ability of active locomotion. That is, the CR can move forward and backward to enable a second inspection for a missed lesion, stop at any locations of interest to make a definite diagnosis or release a drug, and expand collapsed regions for better visualization. The implementation of this complete ability relies on the adopted locomotion mechanism (LM). A variety of LMs, typically as the paddle-type [13], tank-like [14], spiral-type [15], vibration-based [16], superelastic-legged [17], and inchworm-like [18], have been developed during the past decade, while only the inchworm-like LM achieves this complete ability in a reasonable manner. Even so, the inchworm-like LM still has a limitation that its body needs elongation and retraction to enable active locomotion, which has been proven adverse for the CR to achieve a high locomotion efficiency [19].

The second feature is that the CR should be tether-less to avoid possible locomotion failure caused by a friction between a tether and the intestine. The tether-less feature requires that a control command and a captured intestinal image/video should be transmitted wirelessly, which has been implemented in a previous work [20]. It also makes the power supply for the CR a challenging issue, because a button battery currently available for integration has a quite limited capacity and can't power the CR for a long duration. A promising solution to this issue is wireless power transmission (WPT) based on inductive coupling principle [21], [22]. WPT is normally implemented with a 1-D transmitting coil for exciting alternating magnetic field in a patient's abdominal area, and a 3-D receiving coil onboard the CR for induction. Because the available space in the CR is quite limited, how to design a 3-D receiving coil that can induce sufficient electric power for CR operation, serves as a key difficulty for implementing WPT. To solve this difficulty, several studies have been conducted. Carta *et al.* [23] proposed a method of inserting a ferrite core within the receiving coil, which has been proven to double the induced power within a halving volume. Gao et al. designed a hollow-cylinder 3-D receiving coil which was dedicated for being integrated to the inchworm-like CR to improve space utilization, and it has been proven to induce sufficient electric power with a minimum of 485.7 mW at the worst case [18]. With reference to electromagnetic theory, a calculation-based design method for a circular-type 1-D receiving coil has been proposed, which provided effective guidance for selecting design parameters [24] and laid a foundation for the rapid design of the receiving coil. Despite the above achievements, a calculation-based design method dedicated for a solid-cylinder 3-D receiving coil, which is most commonly used for powering the actuator-based CR, is not available yet. Its design parameters are selected based on experimental comparison currently, which is low efficiency and high cost [25].

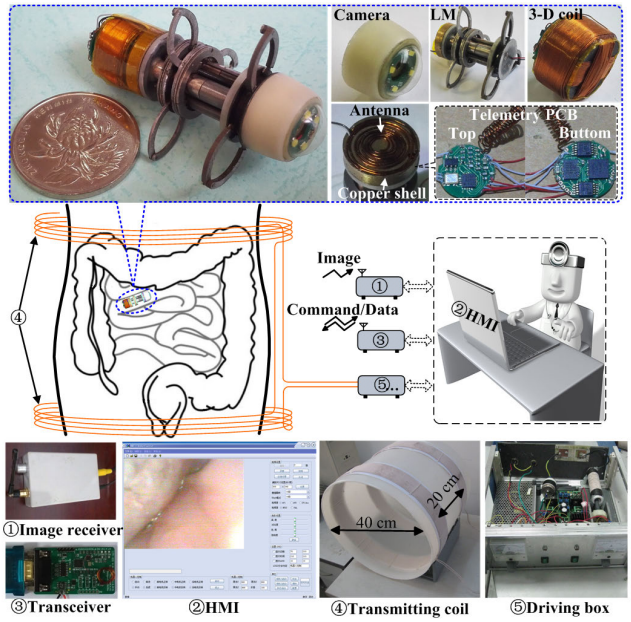

FIGURE 1. Overall design of the CMCR: The upper shows the developed prototype, the middle shows the application scenario, and the lower shows other essential modules for application.

This paper presents the design and implementation of a clamper-based and motor-driven capsule robot (CMCR) that possesses the above two ideal features. Differently from the inchworm-like CR whose LM needs elongation and retraction, the CMCR holds its length but relies on a clamper-based LM to enable active locomotion, therefore it is more promising to achieve a high locomotion efficiency. The main contributions of this paper include:

1) The CMCR shown in Fig. 1, is the first fully integrated device that implements the clamper-based locomotion principle correctly, as compared to a previously developed prototype which is solely a LM and at a proof-of-principle stage [26].
2) The CMCR achieves a compact size by adopting ingenious mechanical design.
3) A calculation-based design method dedicated for the solid-cylinder 3-D receiving coil, which is employed to power the CMCR, is developed for the first time.
4) Two locomotion modes are designed for the CMCR to improve its exploration efficiency in the intestine.

This paper is organized as follows: Section II describes the overall design of the CMCR, Section III details the mechanical design, Section IV optimizes the solid-cylinder 3-D receiving coil, Section V validates the CMCR performance, and Section VII concludes.

II. OVERALL DESIGN

Fig. 1 shows the overall design of the CMCR, which consists of a front-facing camera, a clamper-based LM, a solid-cylinder 3-D receiving coil together with a matched rectification PCB (not shown), and a telemetry printed circuit

TABLE 1. Design specifications of the CMCR.

CMCR	Overall size	Φ 14 mm × 46.8 mm
	Weight	21.48 g
	Total power demand	~ 0.504 W
Camera [27]	Size	Φ 14 mm × 8 mm
	Resolution	320 × 240 dpi
	Power demand	0.064 W
Clamper-based LM	Size	Φ 14 mm × 23 mm
	Periodic stroke S_T	14.5 mm
	Expanding range	Φ (14-31) mm
	Power demand	~ 0.4 W
Telemetry PCB	Size (Copper shell)	Φ 13.6 mm × 4 mm
	Power demand	0.04 W
Solid-cylinder 3-D coil	Size	Φ 13.6 mm × 10 mm
Rectification PCB	Size	Φ 10 mm × 1.8 mm

board (PCB) that is housed in a copper shell, with design specifications as listed in Table 1.

The camera, which can capture an intestinal image with a resolution of 320 × 240 dpi, uses a CMOS sensor OV6922 (Omnivision) that is controlled by a MCU PIC12F509 (Microchip). The image is then wirelessly transmitted (at a frequency of 870 MHz) to a commercialized image receiver for display on a HMI. This camera has been verified to capture clear intestinal images in an alternating magnetic field with a transmission frequency of 218 KHz [27].

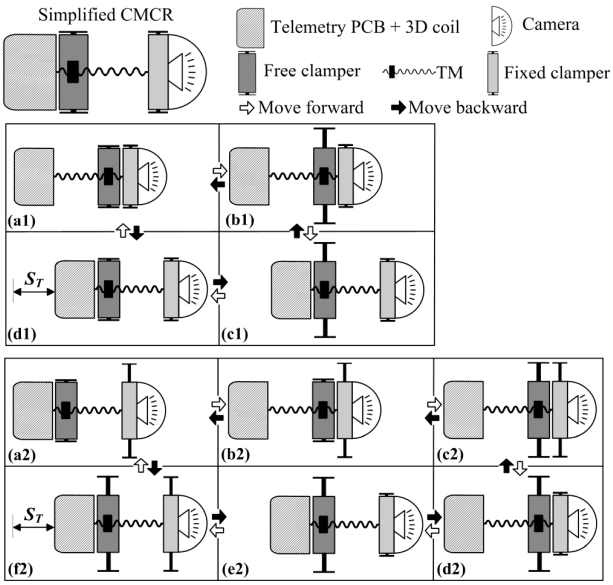

FIGURE 2. Four- and six-gait modes of the CMCR locomotion.

The clamper-based LM has a compact size of Φ14 mm × 23 mm, and it consists of three sub-mechanisms: a translational mechanism (TM), a free clamper that can be moved linearly by the TM, and a fixed clamper. Each sub-mechanism employs a motor for actuation. Two modes are designed for the CMCR locomotion, as shown in Fig. 2: the six-gait mode, in which the CMCR clamps the intestine all the time, is used when the CMCR moves against GI peristalsis or climbs a sloped intestine; while the four-gait is used in other cases to improve velocity.

The solid-cylinder 3-D receiving coil can induce electric power from an alternating magnetic field which is excited by a transmitting coil and a driving box. The transmitting coil, measuring Φ40 cm × 20 cm, is a pair of double-layer solenoid constructed with 180/38 litz wire, and the number of turns of each layer is 25. The driving box integrates a full-bridge inverter and is in charge of converting a DC supply power voltage to an AC voltage. When the AC voltage is loaded on the transmitting coil, the alternating magnetic field can be excited. To avoid adverse health effect caused by the alternating magnetic field, the amplitude of the driving current flowing in the transmitting coil must be limited, which should not exceed an upper limit of 1.98 A when the transmission frequency is 218 KHz [24]. Design details of the transmitting coil and the driving box could refer to a previous study [28].

The telemetry PCB integrates: a MCU PIC16F690 (Microchip), a voltage regulator LT1763 (Linear), two motor drivers AT5550 (Aimtron), a wireless communication chip Si4455 (Silicon Labs) working at 433 MHz for command/data interaction with an external transceiver, and a current-sense chip MAX4173 (Maxim) for detecting the motor current to achieve a closed-loop control [18]. To avoid electromagnetic interference caused by the alternating magnetic field, the telemetry PCB is wholly housed in a copper shell except an antenna matched with the chip Si4455.

The application scenario of the CMCR is as follows. First, the patient ingests the CMCR and put himself within the transmitting coil. Next, the doctor controls the transmitting coil to excite an alternating magnetic field, from which the solid-cylinder 3-D receiving coil induces electric power and powers the CMCR to work. Then, the doctor analyzes the intestinal image that is captured by the camera and displayed on the HMI, and issues a command to control the CMCR to execute specific task via the transceiver and the telemetry PCB. Finally, the CMCR exits from the anus, and it can be reused after cleaning and sterilization.

III. DESIGN OF CLAMPER-BASED LM

A. DESIGN OF TM

Fig. 3 shows the design details of the TM, and its design parameters are listed in Table 2. The TM is implemented with a pair of lead-screw and nut that is actuated by a planetary reducer motor (PRM). To transmit the output torque of the PRM to the lead-screw, three super gears are employed, i.e., SG17 (SG denotes spur gear, 17 denotes teeth number) connecting the PRM, SG10, and SG8 connecting the lead-screw. By placing the nut within the free clamper, the TM can move the CMCR or the free clamper alternatively, depending on the state of the free clamper, as shown in Fig. 2. When the free clamper expands and clamps the intestine, the CMCR will be moved by the lead-screw; otherwise, the free clamper will be moved by the nut. To avoid possible short-circuit fault of the

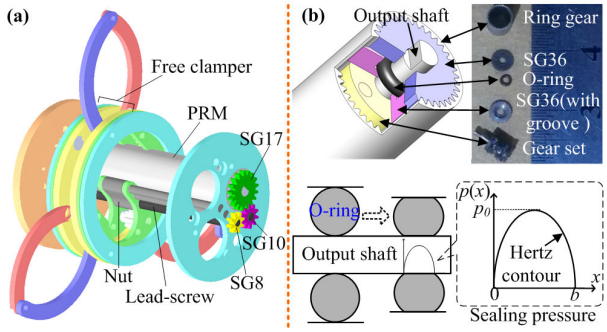

FIGURE 3. (a) Mechanical design of the TM. (b) Sealing design of the PRM.

TABLE 2. Design parameters of the TM.

PRM	Size	Φ 4 mm × 19 mm
	Power demand	3.3 V × 120 mA
	Reduction ratio	64
	Stall torque	M_{TM} =76.27 gf · cm
Lead-screw	Nominal diameter	d_{l-s} =1.2 mm
	Thread angle	β_{TM} =60°
	Pitch	p_{TM} =0.25 mm
	Friction coefficient with nut	μ_{TM} =0.15
	Helix angle	$\psi = \arctan(p_{TM}/\pi d_{l-s})$
	Equivalent friction angle	$\rho_v = \arctan(\mu_{TM}/\cos(\beta_{TM}/2))$
Nut	Length	L_{nut} =2.4 mm
Three super gears: SG17, SG10, SG8	Modulus	0.2 mm
	Reduction ratio	n_{TM} =0.47
	Transmission efficiency	η_{TM} =0.94

PRM in the water-rich intestine, an O-ring (inner diameter 1 mm, wire diameter 0.5 mm, hardness 60) is used to seal its output shaft (diameter 1.05 mm). Referring to Hertz contact theory [29], the compression ratio of the O-ring is optimized as 10%, which enables a sealing pressure of 663.28 Kpa (larger than the required 200 Kpa [30]) and only causes a small torque loss (denoted with M_O) of 0.138 gf·cm. Identical sealing design has also been adopted by the PRMs of the free and fixed clampers.

The longitudinal thrust of the TM can be calculated as:

$$F_{TM} = \frac{2(M_{TM} - M_O)n_{TM}\eta_{TM}}{d_{l-s}[\tan(\psi + \rho_v) + \frac{\mu_{TM}\pi a}{L_{nut}\sin(\beta_{TM}/2)}]} - F_f, \quad (1)$$

where $M_{TM}, n_{TM}, \eta_{TM}, d_{l-s}, \psi, \rho_v, \mu_{TM}, L_{nut}, \beta_{TM}$ have been defined in Table 2; $a = 2.5$ mm is the distance between the center line of the lead-screw and that of the CMCR; F_f is the axial friction when the free clamper is moved linearly, and it is measured as 0.36 N. With the design parameters given in Table 2, the TM can generate a longitudinal thrust $F_{TM} = 4.49$ N, which is sufficient to overcome intestinal resistance in most cases.

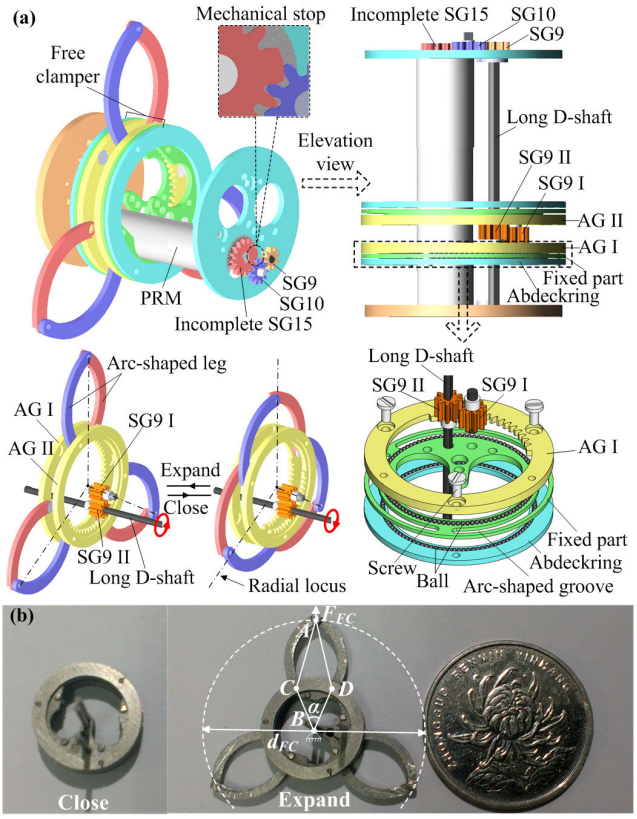

FIGURE 4. (a) Mechanical design of the free clamper. (b) The assembled prototype.

TABLE 3. Design parameters of the free clamper.

PRM	Size	Φ 4 mm × 19 mm
	Power demand	3.3 V × 120 mA
	Reduction ratio	256
	Stall torque	M_{FC} =224.65 gf · cm
Incomplete SG 15, SG 10, SG 9, SG9 I and II, AG I and II	Modulus	0.2 mm
	Reduction ratio	n_{FC} =3.6
	Transmission efficiency	η_{FC} =0.68
Expanding force	$F_{FC} \geq 4.17$ N when 14 mm $\leq d_{FC} \leq$ 31 mm	
Thickness	5 mm	

B. DESIGN OF FREE CLAMPER

The design of the free clamper is a challenging issue because it is required to expand the intestine that has a diameter range of 20 mm to 30 mm, and at the same time, it can be moved linearly by the TM. In addition, the thickness of the free clamper should be as small as possible to increase the periodic stroke, as shown in Fig. 2. Given the above, the free clamper adopted two annular gears (AGs) and three pairs of arc-shaped legs for expansion, as shown in Fig. 4; and its design parameters are listed in Table 3.

As in Fig. 4(a), the PRM of the free clamper is placed at a position complementary to that of the TM (see Fig. 3(a)),

and its output torque is transmitted to a long D-shaft by three spur gears, i.e., incomplete SG 15 connecting the PRM, SG 10, and SG 9 connecting the long D-shaft. To transmit the torque from the long D-shaft to AG I and AG II, SG9 I and SG9 II are employed: SG9 I is meshed with AG I and SG9 II simultaneously; while SG9 II is set at the long D-shaft with a D-hole, and it is meshed with AG II. In this way, AG I and AG II will rotate in reverse and at the same speed when the long D-shaft rotates, thus driving the three pairs of arc-shaped legs to expand/close along a radial locus (the red legs are hinged at the lateral surface of AG I and the blue ones at that of AG II). The incomplete SG 15 plays a mechanical stop function, when it rotates clockwise/anticlockwise to the terminal, the free clamper fully expands/closes.

To ensure AG I and AG II can rotate stably and can be linearly moved by the TM, two extra parts, a fixed part and an abdeckring, are designed, as shown at the lower left of Fig. 4(a). Take AG I as an example, by assembling with the fixed part and the abdeckring using three screws, AG I rotate together with the abdeckring along the arc-shaped groove of the fixed part, and can be linearly moved together with the fixed part by the TM. To minimize torque loss caused by friction, balls with 0.35-mm diameter are set between each two of AG I, the fixed part, and the abdeckring.

Fig. 4(b) shows the assembled prototype of the free clamper, it has a thickness of 5 mm and an expanding diameter range of 14 mm to 31 mm. Its expanding force F_{FC} is a function of its expanding diameter d_{FC}:

$$F_{FC} = \frac{M_{FC} n_{FC} \eta_{FC}}{d_{FC} BD^2} \times \sqrt{d_{FC}^2 (AD^2 + BD^2)/2 - (AD^2 - BD^2)^2 - d_{FC}^4/16}, \quad (2)$$

where M_{FC}, n_{FC}, η_{FC} have been defined in Table 3, AD(= 10.4 mm) is the straight length of the arc-shaped leg, BD(= 6.55 mm) is the distance between the center of AG I/II and the hinged point of the arc-shaped leg. Using Eq. (2) and the design parameters listed in Table 3, we find that when d_{FC} is in the range of 14 mm to 31 mm, F_{FC} is always larger than 4.17 N, sufficient to expand the collapsed intestine.

C. DESIGN OF FIXED CLAMPER

The fixed clamper adopts identical expansion design with the free clamper, but employs a more compact design and achieves a smaller thickness of 2.5 mm. Fig. 5 shows its design details, and the design parameters are listed in Table 4. As in Fig. 5(a), the PRM of the fixed clamper is placed in parallel with those of the TM and the free clamper. To transmit the output torque of the PRM to AG III and AG IV, four supr gears, i.e., SG 18 that connects to the PRM and is meshed with AG III, two SGs 10, and SG 16 that is meshed with AG IV, are employed. The arc-shaped legs are hinged at the bulges machined on the outer surface of AG III (IV), and this design reduces the thickness of the fixed clamper by 1.5 mm as compared to that of the free clamper. The expanding/closing

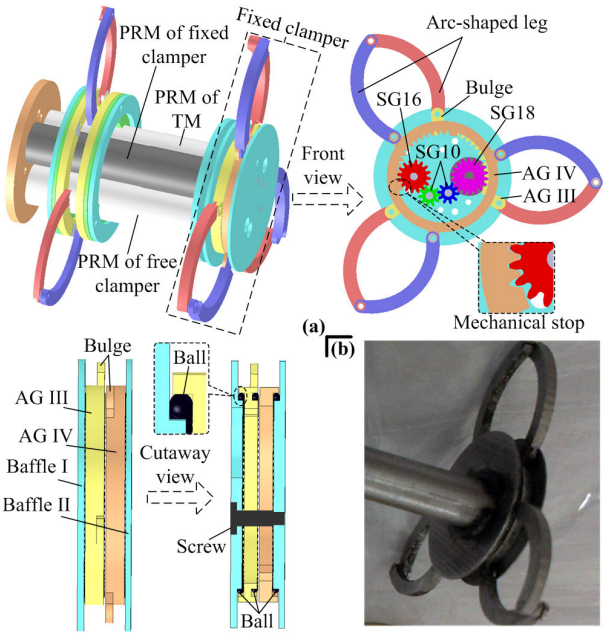

FIGURE 5. (a) Mechanical design and (b) assembled prototype of the fixed clamper.

TABLE 4. Design parameters of the fixed clamper.

PRM	Identical with that of the free clamper	
SG 18, AG III and IV	Modulus	0.2 mm
	Reduction ratio	n_{FC} =2.56
	Transmission efficiency	η_{FC} =0.89
Expanding force	$F_{FC} \geq 3.88$ N when 14 mm $\leq d_{FC} \leq$ 31 mm	
Longitudinal thickness	2.5 mm	

state of the fixed clamper is also controlled in a mechanical stop manner, by adopting incomplete AG III (IV). To ensure AG III (IV) can rotate stably, baffle I (II) having a 0.25-mm high lug boss, is designed. The lug boss matches with a 0.25-mm deep groove machined on one side of the AG III (IV), and balls with 0.35-mm diameter are set between them as supports. The balls are also set between AG III and AG IV for friction reduction. Fig. 5 (b) shows the assembled prototype of the fixed clamper. Its expanding force, which can also be calculated with Eq. (2), is larger than 3.88 N in the expanding diameter range of 14 mm to 31 mm, also sufficient to expand the collapsed intestine.

IV. DESIGN OF SOLID-CYLINDER 3-D RECEIVING COIL

A. GEOMETRIC PARAMETER DEFINITION AND WINDING RULE

The solid-cylinder 3-D receiving coil is composed of a rectangular coil a, a rectangular coil b, a circular coil c, and a cylindrical ferrite core having several grooves on its lateral and end faces, as shown in Fig. 6. Table 5 defines the geometric parameters labelled in Fig. 6. Note that the groove size is in a certain proportion to the ferrite core size, and this proportion

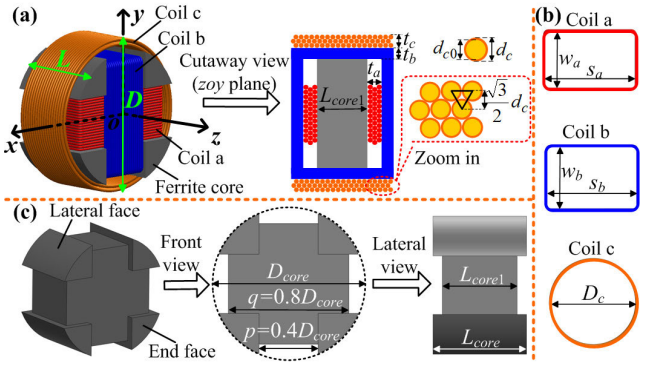

FIGURE 6. (a) Design showing of the solid-cylinder 3-D receiving coil. (b) Geometric parameters of coils a, b, and c. (c) Geometric parameters of the ferrite core.

is from practical experience to ensure winding spaces for coils a and b are sufficient. The winding rules are as follows:

(1) Coils a, b, and c are wound tightly, and the winding wires at different layers are staggered, as shown in Fig. 6(a).

(2) Coils a and b are wound as closely as possible to the groove width of the ferrite core, coil c is wound as closely as possible to the length of the ferrite core. Under this rule, the single-layer numbers of turns of coils a, b, and c can be calculated with the formulas listed in Table 5, respectively.

B. WPT MODEL

By simplifying the transmitting coil and the solid-cylinder 3-D receiving coil with single-turn models, the relative position between them can be described with an axial offset A_0, a radial offset $R_0 = 0$, and an attitude function $g_i(i = a, b, c)$, as shown in Fig. 7. Note that the attitude function g_i reflects the attitude of coil i ($i = a, b, c$) relative to the central axis of the transmitting coil (i.e., the OZ axis): when coil i is perpendicular to the OZ axis, $g_i = 1$; when parallel, $g_i = 0$; and at other cases, $0 < g_i < 1$. Assuming a driving current $I_t = I_m \sin(2\pi ft)$ flows through the transmitting coil, the solid-cylinder 3-D receiving coil will induce an electric power P, which can be calculated as follows when coils a, b, and c are connected in parallel:

$$\begin{aligned} P &= \max[P_i] \\ P_i &= \varepsilon_i^2 R_L/(R_i + R_L)^2 \quad (i = a, b, c) \\ \varepsilon_i &= \sqrt{2}\pi N_i M_i g_i(\theta_1, \theta_2) I_m f \end{aligned} \tag{3}$$

where P_i, ε_i, R_i, N_i are the induced power, induced EMF, equivalent series resistance (ESR), and number of turns of coil i, respectively. M_i is the single-turn mutual inductance between coil i and the transmitting coil. R_L is the load resistance which typically has a value of 21.6 Ω. It can be found from Eq. (3) that to correlate the electric power P with the selectable design parameters (including the number of turns and wire diameter of coil i, and the ferrite core size), M_i and R_i should be calculated firstly.

TABLE 5. Geometric parameters of the solid-cylinder 3-D receiving coil.

Available space	Diameter	D
	Length	L
Ferrite core	Diameter	D_{core}
	Length	$L_{core} = L$
	Groove width	$p = 0.4\ D_{core}$
	Distance between two grooves on lateral face	$q = 0.8\ D_{core}$
	Distance between two grooves on end face	$L_{core1} = L - 0.3D_{core}$
Coil a	Bare copper wire diameter	d_{a0}
	Wire diameter with insulation	$d_a = 0.09796(d_{a0}/0.079)^{0.94}$
	Single-layer number of turns	$N_{as} = \lfloor p/d_a \rfloor$
	Number of layers	N_{al}
	Total number of turns	$N_a = N_{as} \times N_{al}$
	Thickness	$t_a = \sqrt{3}(N_{al} - 1)d_a/2 + d_a$
	Length of single turn (average)	$s_a = q + t_a$
	Width of single turn (average)	$w_a = L_{core1} + t_a$
Coil b	Bare copper wire diameter	d_{b0}
	Wire diameter with insulation	$d_b = 0.09796(d_{b0}/0.079)^{0.94}$
	Single-layer number of turns	$N_{bs} = \lfloor p/d_b \rfloor$
	Number of layers	N_{bl}
	Total number of turns	$N_b = N_{bs} \times N_{bl}$
	Thickness	$t_b = \sqrt{3}(N_{bl} - 1)d_b/2 + d_b$
	Length of single turn (average)	$s_b = q + t_b$
	Width of single turn (average)	$w_b = L_{core1} + 2t_a + t_b$
Coil c	Bare copper wire diameter	d_{c0}
	Wire diameter with insulation	$d_c = 0.09796(d_{c0}/0.079)^{0.94}$
	Single-layer number of turns	$N_{cs} = \lfloor L_{core}/d_c \rfloor$
	Number of layers	$N_{cl} = \left\lfloor \frac{(D - D_{core})/2}{\sqrt{3}d_c/2} + 1 \right\rfloor$
	Total number of turns	$N_c = N_{cs} \times N_{cl}$
	Thickness	$t_c = \sqrt{3}(N_{cl} - 1)d_c/2 + d_c$
	Diameter (average)	$D_c = D_{core} + t_c$

1) CALCULATION OF MUTUAL INDUCTANCE M_i

The mutual inductance is calculated with reference to the Neumann' formula [31]:

$$M_i = \frac{\mu_i N_t}{4\pi}\left(\oint_{O_{t1}}\oint_{O_i}\frac{dl_{t1}dl_i}{r_{t1-i}} + \oint_{O_{t2}}\oint_{O_i}\frac{dl_{t2}dl_i}{r_{t2-i}}\right) \quad i = a, b, c \tag{4}$$

where μ_i is the effective permeability of the area enclosed by coil i. $N_t(= 25)$ is the number of turns of the transmitting coil. O_{t1} and O_{t2} are two loops which represent the

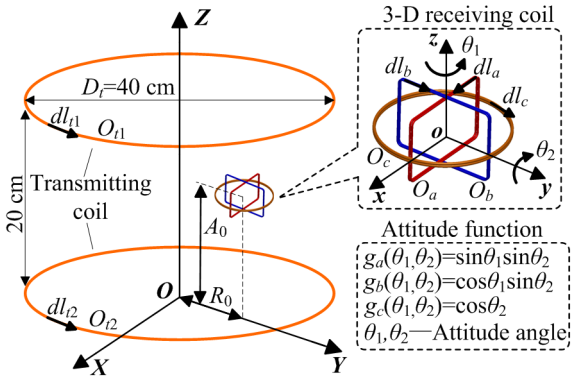

FIGURE 7. Relative position between the transmitting coil and the solid-cylinder 3-D receiving coil.

single-turn model of the transmitting coil shown in Fig. 7, dl_{t1} and dl_{t2} are the infinitesimal elements in loops O_{t1} and O_{t2}, respectively. O_i $(i = a, b, c)$ is the loop which represents the single-turn model of coil i, and dl_i is the infinitesimal element in loop O_i. r_{t1-i} (r_{t2-i}) is the distance between dl_{t1} (dl_{t2}) and dl_i. When the solid-cylinder 3-D receiving coil is set at the center of the transmitting coil (i.e., $A_0 = 10$ cm, $R_0 = 0$), where the magnetic flux density has been verified as the minimum [25], Eq. (4) can be simplified as:

$$M_i \approx 0.25\mu_i N_t D_t^2 w_i s_i / \sqrt{[(D_t/2)^2 + A_0^2]^3} \quad (i = a, b)$$
$$M_c \approx 0.0625\pi\mu_c N_t D_t^2 D_c^2 / \sqrt{[(D_t/2)^2 + A_0^2]^3}. \tag{5}$$

2) CALCULATION OF ESR R_i

The ESR of coil i can be calculated as:

$$R_i = \frac{R_{i-AC}}{(1 - f^2/f_{i-self}^2)^2} \approx R_{i-AC} \quad i = a, b, c \tag{6}$$

where R_{i-AC} and f_{i-self} are the AC resistance and self-resonance frequency of coil i, respectively. Because the transmission frequency of the employed transmitting coil ($f = 218$ KHz) is much lower than f_{i-self} which is normally at several MHz, R_i is nearly equal to R_{i-AC}:

$$R_{i-AC} = R_{i-coil} + R_{i-core} \quad i = a, b, c \tag{7}$$

where R_{i-coil} is the resistance accounting for skin and proximity loss of coil i, R_{i-core} reflects the magnetic loss in the ferrite core corresponding to coil i. Calculations of R_{i-coil} and R_{i-core} could refer to a previous study [24].

3) CALCULATION-BASED OPTIMIZATION DESIGN

Based on the above calculations, the solid-cylinder 3-D receiving coil can be designed with the flow shown in Fig. 8. Here, coils c, a, b are optimized in sequence because the design parameters of the later have dependencies on those of the former. To be specific, when available space has been given and under the winding rules (1) and (2): coil c can be uniquely determined by d_{c0} and D_{core}; coil a can be uniquely determined by D_{core}, d_{a0}, and N_a; and coil b can be uniquely determined by D_{core}, d_{a0}, N_a, d_{b0},and N_b. Therefore, these six design parameters are selected as the objects to be optimized. When conducting optimization, Eqs (3)-(7) are used to optimize these objects to achieve the goals of maximizing P_c, P_a, and P_b orderly. Considering that P_a, P_b, and P_c should be close to each other to reduce the output power fluctuation of the solid-cylinder 3-D receiving coil at any attitude, two judgments concerning the differences between each two of them are set in the design flow. When the difference is larger than 100 mW, re-optimization is required and increasing D_{core} by a small increment Δ has been verified as an effective method for difference reduction.

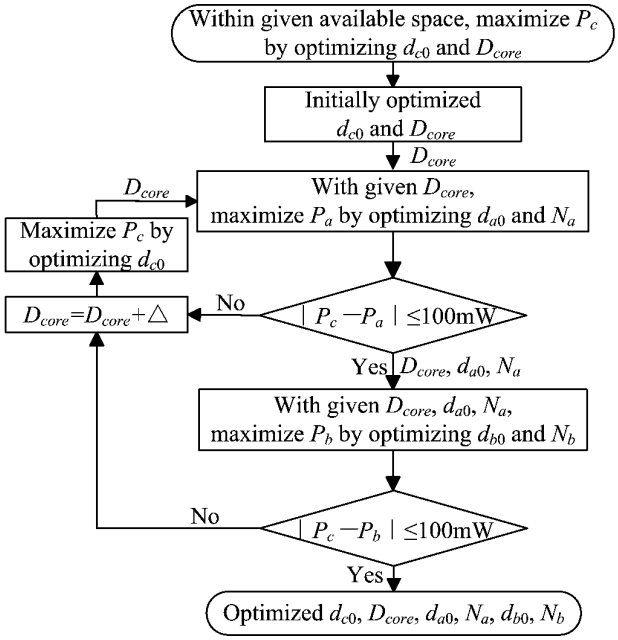

FIGURE 8. Design flow of the solid-cylinder 3-D receiving coil.

To better understand the proposed design flow shown in Fig. 8, the changing of P_c, P_a, and P_b with the design parameters to be optimized, is observed, as shown in Fig. 9. Here, the size of the given available space is $D = 14$ mm, $L = 10$ mm; the selected wire diameters are all commercial available and are all smaller than the skin depth of the copper at 218 KHz. Fig. 9(a) shows that P_c firstly increases with then decreases rapidly with D_{core}, and the maximum of P_c for different d_{c0} is mostly achieved when D_{core} is in the range of 11 mm to 13 mm. When D_{core} has increased to nearly the upper limit $D = 14$ mm, N_c will decrease rapidly because of the limited winding space, which accounts for the rapid decrease of P_c after it has achieved the maximum. Figs. 9 (b) and (c) shows that P_a and P_b have similar changing trend with the increase of N_a and N_b, respectively. When $d_{a0} \le 0.15$ mm, P_a firstly increases then decreases with N_a, this is because ε_a and R_a both increase with N_a, meaning an optimal N_a exist which enables a maximal P_a, as referred to Eq (3). When $d_{a0} \ge 0.18$ mm, N_a is limited by the winding

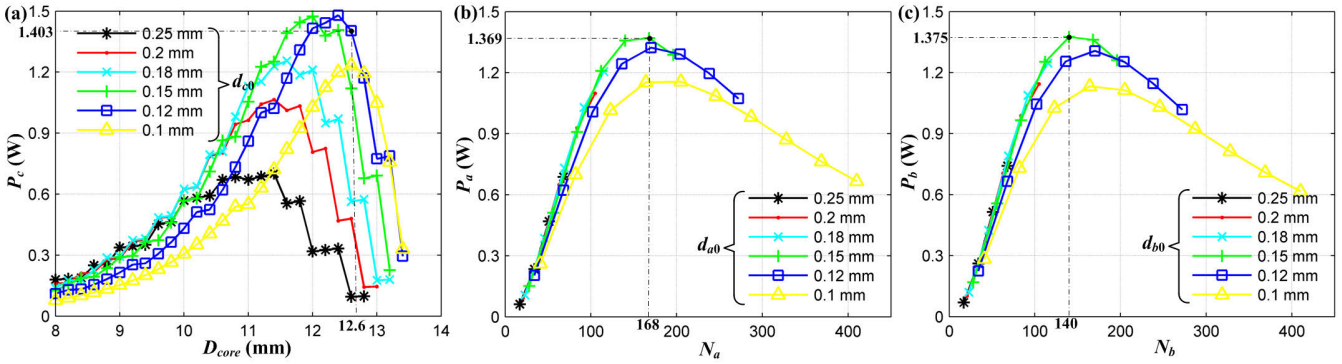

FIGURE 9. Changing of P_c, P_a, and P_b with the design parameters to be optimized, when the size of available space is $D = 14$ mm, $L = 10$ mm.

TABLE 6. Optimized design parameters of the solid-cylinder 3-D receiving coil.

Ferrite core	Diameter D_{core}	12.6 mm
	Length L_{core}	10 mm
Coil a	Bare copper wire diameter d_{a0}	0.15 mm
	Total number of turns N_a	168
	Thickness t_a	0.954 mm
	Induced power $P_a\|_{g_a=1}$ (theoretical)	1.369 W
Coil b	Bare copper wire diameter d_{b0}	0.15 mm
	Total number of turns N_b	140
	Thickness t_b	0.799 mm
	Induced power $P_b\|_{g_b=1}$ (theoretical)	1.375 W
Coil c	Bare copper wire diameter d_{c0}	0.12 mm
	Total number of turns N_c	272
	Thickness t_c	0.522 mm
	Induced power $P_c\|_{g_c=1}$ (theoretical)	1.403 W

space, thus making P_a can't achieve its maximum, therefore a copper wire having a d_{a0} larger than 0.18 mm is not fit to wind coil a here. Similarly, a d_{b0} larger than 0.18 mm is also not fit to wind coil b.

Using the design flow shown in Fig. 8, and referring to the changing trends of P_c, P_a, and P_b shown in Fig. 9, the design parameters of the solid-cylinder 3-D receiving coil are optimized, which are listed in Table 6 and labelled in Fig. 9. The upper left of Fig. 10 shows a fabricated prototype using the optimized design parameters, with a size of Φ13.6 mm $\times$ 10 mm. To measure the induced power of the prototype at any attitude, a two-axis turntable is used and the measuring method is detailed in a previous study [18]. Fig. 10 shows the measuring results when setting: driving current amplitude $I_m = 1.98$ A, transmission frequency $f = 218$ KHz, and load resistance $R_L = 21.6\ \Omega$. It can be found that the measured $P_a\,|_{g_a=1}$, $P_b\,|_{g_b=1}$, and $P_c\,|_{g_c=1}$ are close to each other and are basically smaller than their theoretical values, having a maximum deviation of 0.117 W (for $P_a\,|_{g_a=1}$).

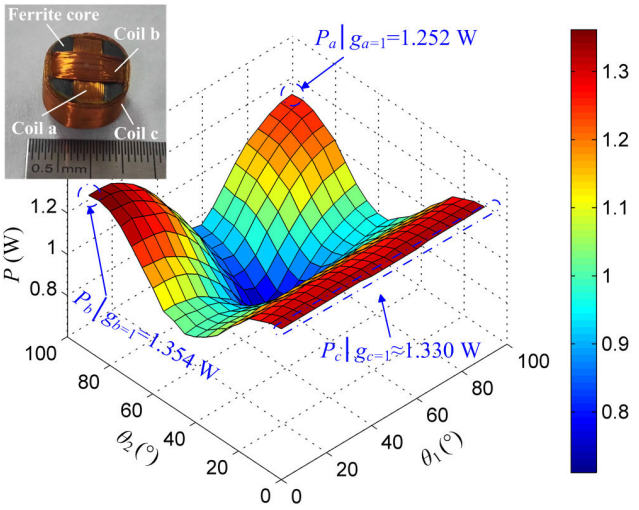

FIGURE 10. Prototype of the solid-cylinder 3-D receiving coil and measuring results of its induced power at any attitude.

Considering manual winding error and approximate calculation of ESR in the WPT model, this deviation is in a tolerable range. Therefore, the proposed calculation-based design flow is effective for optimizing the design parameters of the solid-cylinder 3-D receiving coil. The worst output power is 0.711 W ($\theta_1 = 50°$, $\theta_2 = 60°$), larger than the total power demand of the CMCR ($\sim$0.504 W), thus ensuring its functioning properly.

V. EXPERIMENTS

A. TEST IN A TRANSPARENT TUBE

To assess long-time working reliability of the CMCR powered by WPT, a test in a transparent tube was conducted. The transparent tube, having an inner diameter of 24 mm, was placed in the transmitting coil. Using the HMI, transceiver, and telemetry PCB shown in Fig. 1, the CMCR was wirelessly controlled to perform actions continuously, for a long duration of 3 hours. Fig. 11 shows the gait snapshots when the CMCR moved forward in the six-gait mode, which were finely corresponded to those shown in Fig. 2. The gait transition was implemented with a closed-loop control scheme

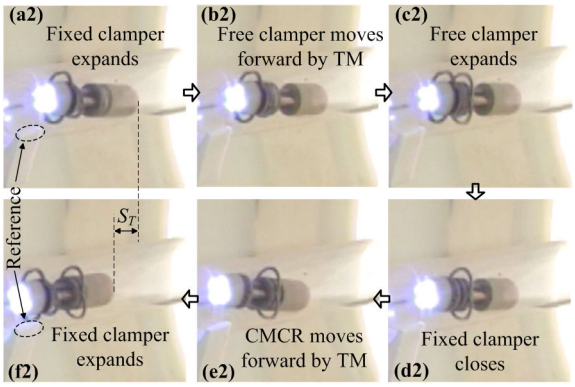

FIGURE 11. Gait snapshots when the CMCR moved forward in a transparent tube.

employing the stall current (detected by the chip MAX4173) of the PRM as a feedback. During the 3-hour test: the fixed and free clampers expand/close smoothly all the time; the TM jammed frequently at first, after carburizing the long D-shaft and polishing its surface to shine with dark metallic luster, the jam occurrence rate was reduced to less than 7%. The CMCR was examined after this test: all the modules remain largely intact except the lead-screw of the TM, whose thread was lightly scuffed, about 0.2 mm at each end. Therefore, a carburizing process is also necessary for the lead-screw to improve its abrasion resistance. During the above test, the communication error rate was about 5% at a communication distance of 2 m. In the case of successful communication, the time interval from the HMI issued a command to the CMCR began to execute it was less than 1 s. The above results showed that the developed CMCR has good mechanical reliability, and it can be controlled reliably and in real-time when powered by WPT.

B. TEST IN EX-VIVO INTESTINE

The test in an ex-vivo intestine was mainly to assess the locomotion performance of the CMCR in four- and six-gait modes. Because slopes existed in vivo, a metal holder, which has two fixtures for holding the intestine in suspended state, was employed here to create angles of the slope ranging from 0° to 90°, as shown in Fig. 12. Note that when the angle of the slope was changed, the horizontal and vertical distances between the two fixtures, both needed to be adjusted to hold the length of the intestine, thus ensuring identical intra-intestinal lumen environment. The ex-vivo intestine had a diameter of about 19 mm and was excised from a pig that weighed roughly 150 kg; it was stored in a refrigerated physiological saline solution to preserve its biomechanical properties before testing. In this testing, the CMCR was connected to an external power using a wire because the metal holder can seriously influence WPT. The intestine was humidified frequently to maintain tissue hydration, and was replaced with a new one every half hour considering that the intestinal tissue stiffened with time in air. At each angle of slope, the CMCR was controlled to move in four-gait mode

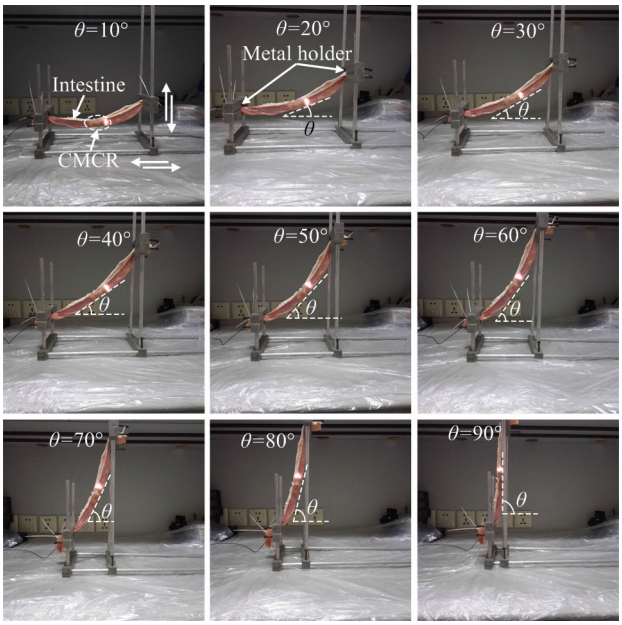

FIGURE 12. Locomotion performance test of the CMCR in sloped intestines.

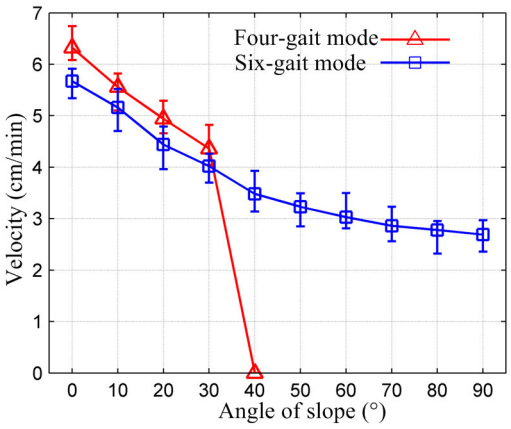

FIGURE 13. Average velocity of the CMCR in sloped intestines, the error bars reflect the measured maximum and minimum velocities in each set of test.

for 3 times, then in six-gait mode for 3 times. Fig. 13 showed the testing results, which can be concluded as follows.

First, the CMCR velocity decreases with the angle of the slope, this is because the axial component of the CMCR gravity acts as a resistance when it climbs, which reduces the achieved periodic stroke by causing axial deformations of the intestine [32]. However, as the increase of the angle of the slope, the velocity decreases more and more slowly. We infer this is related to the nonlinear stress-strain relations of the intestine, as indicated by the hyperelastic constitutive equation [33] that the increase of the intestinal strain slows down with the increase of the applied stress.

Second, when the angle of the slope is less than 30°, the CMCR velocities in four-gait mode are basically larger than those in six-gait mode, because the periodic time in four-gait

mode is 1.4 s shorter than that in six-gait mode. When the angle of slope is 40° or larger, the velocity in four-gait mode decreases to zero sharply, and the CMCR was observed to slip when the free and fixed clampers closed. The slip happened because the friction between the CMCR and the intestinal lumen was not sufficient to overcome the axial component of its gravity. To determine the critical angle of the slope that the CMCR began to slip in four-gait mode, the angle of the slope was started with 30° and increased by 1° each time, and a critical value of 36° was obtained. Therefore, to improve the exploration efficiency of the CMCR, the four-gait mode should be adopted when the angle of the slope was less than 36°; in other cases, the six-gait mode should be used.

VI. CONCLUSION

In this paper, a clamper-based and motor-driven capsule robot, i.e., CMCR, has been developed. By employing the clamper-based LM, the CMCR can move forward and backward, stop at locations of interest, and expand collapsed regions in the intestine. By integrating the solid-cylinder 3-D receiving coil and the telemetry PCB, the CMCR can be wireless powered and controlled, respectively. These enable the CMCR has great potential for a thorough inspection of the intestine. Design details of the clamper-based LM have been presented, and it showed high reliability during the 3-hour test: the mechanical jam occurrence rate of the TM was less than 7%, and the free- and fixed-clampers expanded/closed smoothly all the time. The proposed calculation-based design method for the solid-cylinder 3-D receiving coil provides useful guidance for selecting its design parameters, and a fabricated prototype with a size of Φ13.6 mm $\times$ 10 mm can output electric power from 0.711 W to 1.354W, meeting the power demand of the CMCR. The designed four- and six-gait modes ensure the CMCR has a good locomotion performance, as shown in Fig. 13: it achieved a velocity of 6.32 cm/min in a horizontal intestine in four-gait mode, and can even climb in a vertical one with a velocity of 2.69 cm/min in six-gait mode.

Future works focus on identifying the angle of the slope of the intestine in ahead by analyzing the symmetry of the captured intestinal image so that proper locomotion mode can be adopted in advance, and improving the TM design to further lower its jam occurrence rate, these will bring the CMCR one step closer to clinical practice.

REFERENCES

[1] G. Iddan, G. Meron, A. Glukhovsky, and P. Swain, "Wireless capsule endoscopy," *Nature*, vol. 405, p. 417, May 2000.
[2] B. Winstone, C. Melhuish, T. Pipe, M. Callaway, and S. Dogramadzi, "Toward bio-inspired tactile sensing capsule endoscopy for detection of submucosal tumors," *IEEE Sensors J.*, vol. 17, no. 3, pp. 848–857, Feb. 2017.
[3] L. Yan, T. Wang, D. Liu, J. Peng, Z. Jiao, and C.-Y. Chen, "Capsule robot for obesity treatment with wireless powering and communication," *IEEE Trans. Ind. Electron.*, vol. 62, no. 2, pp. 1125–1133, Feb. 2015.
[4] G. Tortora, B. Orsini, P. Pecile, A. Menciassi, F. Fusi, and G. Romano, "An ingestible capsule for the photodynamic therapy of helicobacter pylori infection," *IEEE/ASME Trans. Mechatron.*, vol. 21, no. 4, pp. 1935–1942, Aug. 2016.
[5] L. B. Gerson, "Use and misuse of small bowel video capsule endoscopy in clinical practice," *Clin. Gastroenterol. Hepatology*, vol. 11, no. 10, pp. 1224–1231, Oct. 2013.
[6] A. W. Mahoney and J. J. Abbott, "Five-degree-of-freedom manipulation of an untethered magnetic device in fluid using a single permanent magnet with application in stomach capsule endoscopy," *Int. J. Robot. Res.*, vol. 35, pp. 129–147, Feb. 2015.
[7] C. Lee, H. Choi, G. Go, S. Jeong, S. Y. Ko, J.-O. Park, and S. Park, "Active locomotive intestinal capsule endoscope (ALICE) system: A prospective feasibility study," *IEEE/ASME Trans. Mechatronics*, vol. 20, no. 5, pp. 2067–2074, Oct. 2015.
[8] J.-F. Rey, H. Ogata, N. Hosoe, K. Ohtsuka, N. Ogata, K. Ikeda, H. Aihara, I. Pangtay, T. Hibi, S.-E. Kudo, and H. Tajiri, "Blinded nonrandomized comparative study of gastric examination with a magnetically guided capsule endoscope and standard videoendoscope," *Gastrointestinal Endoscopy*, vol. 75, no. 2, pp. 373–381, Feb. 2012.
[9] W. Lee, J. Nam, B. Jang, and G. Jang, "Selective motion control of a crawling magnetic robot system for wireless self-expandable stent delivery in narrowed tubular environments," *IEEE Trans. Ind. Electron.*, vol. 64, no. 2, pp. 1636–1644, Feb. 2017.
[10] J. Nam, W. Lee, J. Kim, and G. Jang, "Magnetic helical robot for targeted drug-delivery in tubular environments," *IEEE/ASME Trans. Mechatron.*, vol. 22, no. 6, pp. 2461–2468, Dec. 2017.
[11] Y. Zhang, M. Chi, and Z. Su, "Critical coupling magnetic moment of a petal-shaped capsule robot," *IEEE Trans. Magn.*, vol. 52, no. 1, Jan. 2016, Art. no. 5000109.
[12] M. C. Hoang, V. H. Le, J. Kim, E. Choi, B. Kang, J.-O. Park, and C.-S. Kim, "Untethered robotic motion and rotating blade mechanism for actively locomotive biopsy capsule endoscope," *IEEE Access*, vol. 7, pp. 93364–93374, 2019.
[13] H. M. Kim, S. Yang, J. Kim, S. Park, J. H. Cho, J. Y. Park, T. S. Kim, E.-S. Yoon, S. Y. Song, and S. Bang, "Active locomotion of a paddling-based capsule endoscope in an *in vitro* and *in vivo* experiment," *Gastrointestinal Endoscopy*, vol. 72, no. 2, pp. 381–387, Aug. 2010.
[14] L. J. Sliker, M. D. Kern, and M. E. Rentschler, "An automated traction measurement platform and empirical model for evaluation of rolling micropatterned wheels," *IEEE/ASME Trans. Mechatronics*, vol. 20, no. 4, pp. 1854–1862, Aug. 2015.
[15] Y.-T. Kim and D.-E. Kim, "Novel propelling mechanisms based on frictional interaction for endoscope robot," *Tribol. Trans.*, vol. 53, no. 2, pp. 203–211, Jan. 2010.
[16] R. Carta, M. Sfakiotakis, N. Pateromichelakis, J. Thoné, D. P. Tsakiris, and R. Puers, "A multi-coil inductive powering system for an endoscopic capsule with vibratory actuation," *Sens. Actuators A, Phys.*, vol. 172, no. 1, pp. 253–258, Dec. 2011.
[17] P. Valdastri, R. J. Webster, C. Quaglia, M. Quirini, A. Menciassi, and P. Dario, "A new mechanism for mesoscale legged locomotion in compliant tubular environments," *IEEE Trans. Robot.*, vol. 25, no. 5, pp. 1047–1057, Oct. 2009.
[18] J. Gao, G. Yan, Z. Wang, S. He, F. Xu, P. Jiang, and D. Liu, "Design and testing of a motor-based capsule robot powered by wireless power transmission," *IEEE/ASME Trans. Mechatronics*, vol. 21, no. 2, pp. 683–693, Apr. 2016.
[19] J. Gao, G. Yan, Z. Wang, F. Xu, W. Wang, P. Jiang, and D. Liu, "Locomotion enhancement of an inchworm-like capsule robot using long contact devices," *Int. J. Med. Robot. Comput. Assist. Surg.*, vol. 13, no. 2, p. e1759, Jun. 2017.
[20] P. Gao, G. Yan, Z. Wang, K. Wang, P. Jiang, and Y. Zhou, "A robotic endoscope based on minimally invasive locomotion and wireless techniques for human colon," *Int. J. Med. Robot. Comput. Assist. Surg.*, vol. 7, no. 3, pp. 256–267, Sep. 2011.
[21] M. R. Basar, M. Y. Ahmadm, J. Cho, and F. Ibrahim, "Stable and high-efficiency wireless power transfer system for robotic capsule using a modified helmholtz coil," *IEEE Trans. Ind. Electron.*, vol. 64, no. 2, pp. 1113–1122, Feb. 2017.
[22] J. Gao and G. Yan, "A novel power management circuit using a supercapacitor array for wireless powered capsule robot," *IEEE/ASME Trans. Mechatronics*, vol. 22, no. 3, pp. 1444–1455, Jun. 2017.
[23] R. Carta, J. Thoné, and R. Puers, "A wireless power supply system for robotic capsular endoscopes," *Sens. Actuators A, Phys.*, vol. 162, pp. 177–183, Jan. 2010.
[24] J. Gao, G. Yan, Z. Wang, P. Jiang, and D. Liu, "A capsule robot powered by wireless power transmission: Design of its receiving coil," *Sens. Actuators A, Phys.*, vol. 234, pp. 133–142, Oct. 2015.

[25] Z. Jia, G. Yan, H. Liu, Z. Wang, P. Jiang, and Y. Shi, "The optimization of wireless power transmission: Design and realization," *Int. J. Med. Robot. Comput. Assist. Surg.*, vol. 8, no. 3, pp. 337–347, Sep. 2012.
[26] J. Gao, G. Yan, S. He, F. Xu, and Z. Wang, "Design, analysis, and testing of a motor-driven capsule robot based on a sliding clamper," *Robotica*, vol. 35, no. 3, pp. 521–536, Mar. 2017.
[27] B. Zhu, G. Yan, G. Liu, and Y. Shi, "Design of a dual-head video capsule endoscopy system based on wireless power transmission technology," *J. Med. Biol. Eng.*, vol. 2, pp. 1–25, 2014.
[28] J. Zhiwei, Y. Guozheng, J. Pingping, W. Zhiwu, and L. Hua, "Efficiency optimization of wireless power transmission systems for active capsule endoscopes," *Physiol. Meas.*, vol. 32, no. 10, pp. 1561–1573, Aug. 2011.
[29] H.-K. Kim, S.-H. Park, H.-G. Lee, D.-R. Kim, and Y.-H. Lee, "Approximation of contact stress for a compressed and laterally one side restrained O-ring," *Eng. Failure Anal.*, vol. 14, no. 8, pp. 1680–1692, Dec. 2007.
[30] F. Xu, G. Yan, K. Zhao, L. Lu, J. Gao, and G. Liu, "A wireless capsule system with ASIC for monitoring the physiological signals of the human gastrointestinal tract," *IEEE Trans. Biomed. Circuits Syst.*, vol. 8, no. 6, pp. 871–880, Dec. 2014.
[31] Z. Luo and X. Wei, "Analysis of square and circular planar spiral coils in wireless power transfer system for electric vehicles," *IEEE Trans. Ind. Electron.*, vol. 65, no. 1, pp. 331–341, Jan. 2018.
[32] J. Gao and G. Yan, "Locomotion analysis of an inchworm-like capsule robot in the intestinal tract," *IEEE Trans. Biomed. Eng.*, vol. 63, no. 2, pp. 300–310, Feb. 2016.
[33] P. Ciarletta, P. Dario, F. Tendick, and S. Micera, "Hyperelastic model of anisotropic fiber reinforcements within intestinal walls for applications in medical robotics," *Int. J. Robot. Res.*, vol. 28, no. 10, pp. 1279–1288, Oct. 2009.

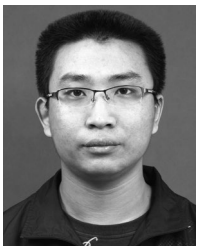

JINYANG GAO was born in Shanxi, China, on October 1, 1990. He received the B.S. degree from the University of Electronic Science and Technology of China, China, in 2012, and the Ph.D. degree from Shanghai Jiao Tong University, Shanghai, China, in 2017. Since 2017, he has been with the North University of China, China. He became an associate professor, in 2019.

He has published ten peer-reviewed articles as the first author and authored eight Chinese invention patents. His research interests include capsule robots, wireless power transmission and related electronic circuit design, and gastrointestinal biomechanics. He received an Honor from the National Excellent Doctoral Dissertation of China in the fields of measurement and control technology and instrument, in 2018.

GUOZHENG YAN was born in Hunan, China, on June 3, 1961. He received the Ph.D. degree from the Jilin University of Technology, Jilin, China, in 1993.

In 1995, he became a Postdoctoral Fellow of the Nanjing University of Aeronautics and Astronautics, China. In 1997, he became a Professor with the Department of Instrument Science and Engineering, Shanghai Jiao Tong University, Shanghai, China. His research interests include biomedical electronics, micro sensors, micro-electromechanical systems, and instrument engineering.